

Microstructure and Properties of Co-Ni-Al-W γ/γ' Superalloy Fabricated via Laser Fusion of Elemental Powders

Hye Ji Im¹, Júlio C. Pereira dos Santos², Carelyn E. Campbell², David C. Dunand^{1*}

¹Department of Materials Science & Engineering, Northwestern University, IL 60208, USA

²National Institute of Standards and Technology, Gaithersburg, MD 20899, USA

*Corresponding author: dunand@northwestern.edu

Ball-milled elemental Co, Ni, Al, and W powders were used to fabricate a Co-0.20Ni-0.11Al-0.08W (mole fraction) alloy *via* laser powder bed fusion (L-PBF). In the as-fused state, microstructural features present within the FCC- γ Co-Ni-Al-W matrix – partially-melted W powders, W-deficient regions, and cracks – are investigated with respect to the laser scanning speed. Tungsten particles appear to block or deflect internal cracks, thus improving cracking resistance due to thermal cycling during laser fusion. However, W-deficient regions, which are also enriched with Ni and Al, can act as crack nucleation sites due to the brittleness of the β -NiAl and eutectic microconstituents. A homogenous FCC- γ Co-0.20Ni-0.11Al-0.08W (mole fraction) solid solution is obtained after a solutionizing treatment at 1200 °C, as W-rich particles fully dissolve, and W-deficient regions homogenize, into the matrix. A γ/γ' -two-phase microstructure forms upon subsequent aging at 900 °C, whose creep resistance is measured at 850 °C: below 300 MPa, deformation is dominated by diffusional creep (consistent with a relatively fine grain size of 50 μm to 100 μm) while above 300 MPa, it is controlled by dislocation creep. Using elemental powder blends is a viable method to create microstructurally-sound, creep-resistant Co-based γ/γ' superalloys *via* L-PBF.

Keywords: Co-based superalloy; selective laser melting; microstructure; crack; creep

1. Introduction

Cobalt-based superalloys are a novel high-temperature alloy family under intense study [1–3] since the 2006 rediscovery of a γ/γ' (disordered FCC (Face Centered Cubic) /ordered L₁₂ FCC phases) metastable microstructure in the Co-Al-W ternary system [4,5]. These Co-based superalloys present excellent corrosion and creep properties at elevated temperature, due to a positive γ/γ' lattice misfit [6] and the higher melting temperature of Co as compared to Ni (1495 °C vs. 1455 °C). Nickel additions to the Co-Al-W system make the γ/γ' region thermodynamically stable and significantly expands its compositional width [7,8]. Ni is also beneficial to the γ' thermal stability and decreases the formation of undesirable, third phases, while enabling additional alloying elements such as Cr, Ti, Ta, Mo, V and Nb that further increase creep- and coarsening resistance while also raising the solvus temperature of these alloys [9,10].

Laser powder bed fusion (L-PBF) is a promising technique for manufacturing components with complex geometries with alloys that have low machinability due to their high hardness, such as turbine blades produced from Ni- and Co-based superalloys [11–13]. However, the rapid solidification and thermal cycling during powder bed fusion (in L-PBF or in closely related directed energy deposition, (DED)) result in unique microstructures with finer length scales and defects (e.g., cracking and lack of fusion)[14,15]. Defects including pores and cracks can

degrade the mechanical properties and limit the wide-scale industrial adoption of this technique to metallic materials. Furthermore, remelting and repeated heating and cooling that occur during the build process results in microsegregation that can promote unexpected phases. Thus, it is crucial to address these defects and present the methods to minimize cracking susceptibility [16,17].

Pre-alloyed powder availability is also a significant barrier for further development of these alloys, which can be bypassed by using blended elemental powders (with or without master alloy powders) as done in a few instances for Ni-based superalloys and Ni-containing multi-principal-element alloys. Ma et al. [18] achieved a homogeneous Fe-15Co-15Ni-10Cr* alloy via L-PBF of blended elemental powders, by using re-scanning or high laser energy input. Their mechanical properties at 77 K were comparable to the same alloy produced by L-PBF with pre-alloyed powder. Chen et al. [19] showed improved elemental homogeneity, including Mn, by re-melting during a L-PBF process using 18.8Co-20.1Cr-20.4Fe-21.4Mn-19.3Ni alloy. Wang et al. [20] demonstrated higher micro-hardness of an Inconel 625 alloy created via DED of blended elemental powders as compared to pre-alloyed powders (339 HV (Hardness Vickers) vs. 298 HV, both measurements were made using the same loads and holding times). Dang et al. [21] improved the thermal stability of the γ'' phase (BCT (Body-Centered Tetragonal) D0₂₂ structure) of Ni-Cr-Al-Ti-Nb alloys by adjusting the concentrations of the γ' - and γ'' -forming elements including Al, Ti and Nb when blending elemental powders.

To our knowledge, only pre-alloyed powders (i.e., not elemental powders) have been used for the additive manufacturing of Co-based superalloys, e.g., Haynes-188 (by L-PBF) [22], Mar-M-509 (L-PBF) [12,23], Co-32Ni-12Al-4W-3Cr-2Ta (L-PBF) [24], and Co-12Al-8W (DED) [13]. The lower powder cost and the greater flexibilities in composition, which is also very useful for rapid development of new alloy compositions [14] motivate this work to demonstrate the use of blended elemental powders for Co-based alloys. However, especially in Co-superalloys based on the Co-Al-W system, the high melting point and density of W are particularly challenging, as these elements make complete melting/dissolution with lack of segregation difficult [25,26].

Here, we demonstrate that a quaternary Co-based superalloy can be fabricated from elemental powders via ball milling and L-PBF, achieving a crack-free and fully-dense alloy. A Co-Ni-Al-W composition was chosen via CALPHAD-based thermodynamic predictions to minimize the freezing range and to achieve an optimal γ (FCC)/ γ' (L1₂) microstructure. We perform microstructural characterization after laser melting, and investigate the dissolution of the high-melting W particles during melting and subsequent homogenization heat-treatments, as well as the evolution of γ' precipitates on aging, and the corresponding creep resistance of the peak-aged γ/γ' alloy.

2. Alloy design and experimental procedures

2.1. Alloy composition

Using the CALPHAD-based CHiMaD-Co thermodynamic database [27,28], the freezing ranges and γ' phase fractions at 900 °C were calculated for the range of compositions in the Co-yNi-xAl-zW space. A composition of Co-20Ni-11Al-8W was chosen based on (i) minimizing the freezing range (the temperature difference between liquidus and solidus temperatures) which reduces cracking propensity during processing [17,29] and (ii)

* All compositions are given in mole fractions times 100, unless otherwise noted.

maximizing γ' phase fraction (which scales with the volume fraction) at the 900 °C aging temperature to improve creep resistance [30,31]. Figure 1(a) shows that the freezing range, calculated using the Scheil model, increases with increasing Ni and Al compositions. On the other hand, the γ' phase fraction in the $\gamma+\gamma'$ dual-phase region, shown in Fig. 1(b), mainly increases with increasing Al and reaches a maximum value of 70 % when Al composition is 11. An intermediate nickel concentration of 20 is chosen, as Ni increases both the freezing range and γ' solvus temperature [32] and widens the compositional window for γ/γ' two-phase region in the Co-Ni-Al-W quaternary system [33].

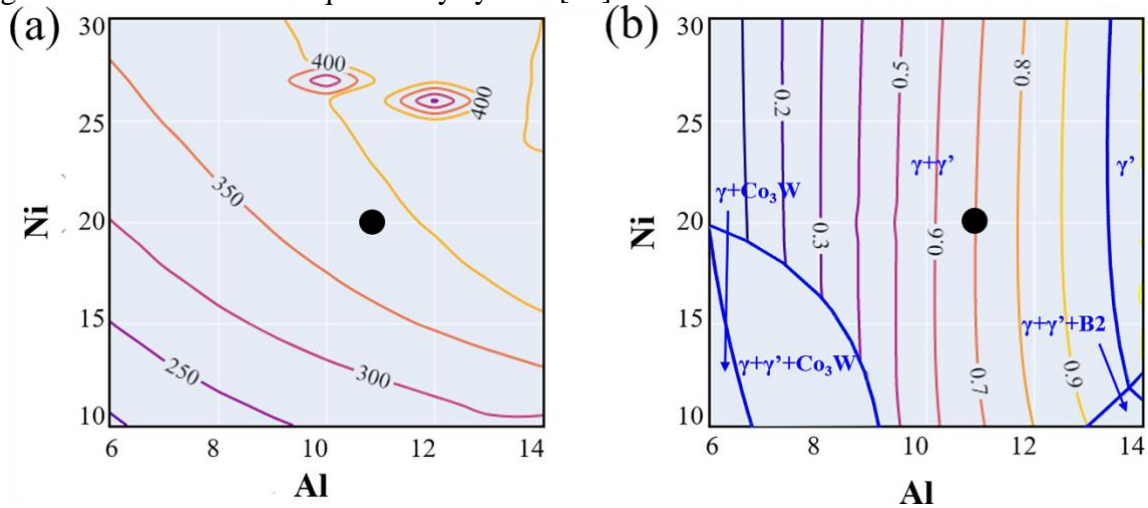


Figure 1. Calculated contour plots of (a) the freezing range, based on Scheil calculations, and (b) γ' phase fraction in $\gamma+\gamma'$ two-phase region at 900 °C as functions of the Ni and Al compositions for the Co-yNi-xAl-8W space (black dot indicates Ni and Al compositions of the investigated alloy).

2.2. Sample fabrication and heat treatments

Figure S1 shows the scheme for the milling process of elemental powders: Co (99.9 %, Stanford Advanced Materials[†]), Ni (99.5 %, US Research Nanomaterials), Al (99.7 %, US Research Nanomaterials), and W (99.95 %, Global Tungsten & Powders) powders. Particle diameter ranges for Co, Ni, and Al are $<45\ \mu\text{m}$, and W powders, sieved through a 400-mesh sieve, are $<20\ \mu\text{m}$. The Ni, Al and W powders were first blended for 5 min in 45 g batches, using a high-energy SPEX mill in Ar with two yttria-stabilized zirconia (YSZ) balls (6.5 mm and 12 mm in diameter). This was carried out before the ball-milling process to minimize inhomogeneous distribution of W powder when mixed with other powders, due to the much higher density of W: this short high-energy milling led to W powders attaching to Ni or Al powders (Fig. 2(a)) which decreased the overall density of the powder agglomerates as compared to pure W powders. The resultant SPEX-milled Ni+Al+W powder was low-energy ball-milled for 4 h with Co powder, using YSZ balls (ball to powder ratio of 1:1) at 6.28 rad/s (60 RPM) under Ar, resulting in homogeneous mixing of the elemental powders and partial mechanical alloying of some W powders with other powders, as shown in Fig. 2(b) and (c).

[†] Certain equipment, instruments, software, or materials are identified in this paper in order to specify the experimental procedure adequately. Such identification is not intended to imply recommendation or endorsement of any product or service by NIST, nor is it intended to imply that the materials or equipment identified are necessarily the best available for the purpose..

The alloys were fabricated from these blended elemental powders using a L-PBF instrument (Sisma MySint 100, Trumpf) equipped with a 200 W fiber-laser operating with a 55 μm spot size. Cubic specimens with a size of $(5 \times 5 \times 5) \text{ mm}^3$ were produced using a bidirectional scan strategy (90° rotation between layers) at scanning speed of 100 mm/s, 200 mm/s, 300 mm/s, and 400 mm/s. Cylindrical creep specimens (11 mm in diameter and 18 mm in height) were produced using an island-scanning strategy at 300 mm/s scanning speed. The XY plane was divided into $(4 \times 4) \text{ mm}^2$ islands with a rotation of 90° for the subsequent island scanning and a 1 mm shift in both the X and Y directions between layers. All creep samples were built at laser power of 200 W, hatch spacing of 105 μm , and a powder layer thickness of 30 μm , under Ar shielding gas ($\text{O}_2 < 100 \text{ ppm}$).

The printed samples were embedded in NiAl powder (to reduce Al losses) within a quartz tube, which was vacuum-sealed, homogenized at 1200 $^\circ\text{C}$ for 96 h (extended to 120 h for creep specimens), and water quenched. Specimens were removed from the partially-sintered NiAl bed and were then aged at 900 $^\circ\text{C}$ for 24 h with a Ti getter-piece in Ar-encapsulated tubes, terminated by water quenching.

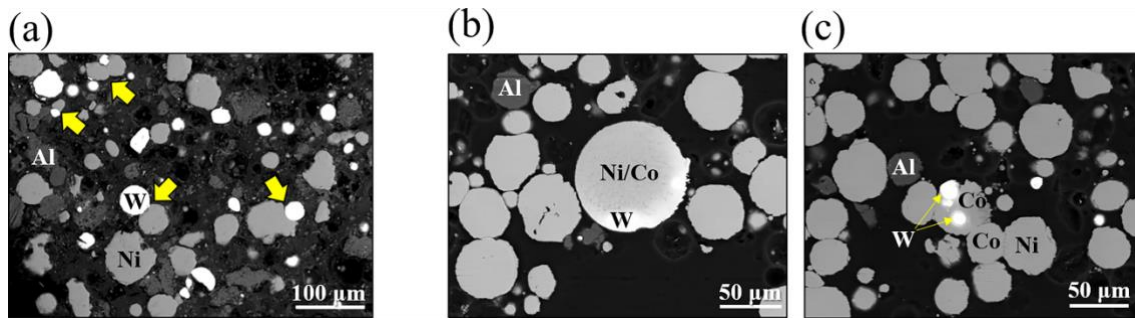


Figure 2. BSE micrographs of powder cross-sections (a) after 5-min SPEX milling (yellow arrows point to attachment of W powders to Ni or Al powders) and (b-c) after 4 h ball milling, showing clearly-identifiable elemental powders as well as partial alloying of W powder in pure Co or Ni powder.

2.3. Microstructural analysis

To measure crack density and determine where cracks end/start within the samples, a vertical section (parallel to the build direction) was obtained from as-deposited samples by half-width cutting and metallographic mounting. The other half was sectioned horizontally (perpendicular to the building direction) into two quarters. Both vertical and horizontal sections were ground, polished (using 3 μm and 1 μm diamond solutions and 0.04 μm colloidal silica suspension), and etched with Carapella's reagent (40 mL ethanol, 40 mL HCl, and 2 g CuCl_2) for 10 s. From vertical and horizontal sections for each sample, about 30 and 15 optical micrographs, respectively, were obtained to measure crack lengths over the whole area. For each image, the regions where cracks are located were isolated and then binarized. Crack length measurements were carried out using Simple Neurite Tracer (SNT) plugin, an open-source software of the ImageJ software. The crack density was obtained by summing crack lengths and then dividing by the whole area of the stitched images of the vertical and horizontal sections.

Micro-features, such as partially-melted W particles and W-deficient regions, were characterized from back-scattered secondary electron (BSE) micrographs, which were taken with a scanning electron microscope (SEM, FEI Quanta 650). The same region imaged via optical microscopy was imaged via SEM at a magnification of 200 times with a constant contrast and brightness value for the whole sample. The area of partially-melted W particles

was obtained by the particle analysis function of ImageJ, using binarized SEM image (size=0-Infinity, circularity=0 to 1.00). The W-deficient regions were identified by the deviation of Z-contrast in the matrix and their area fraction was obtained from histogram analysis of the BSE images using ImageJ. The histograms of W particle-excluded images of all samples were set to saturation value of 0.35 % and equalized, and a threshold value of histogram was used to differentiate the W-deficient regions from the matrix. For histogram values ranging from 0 to 225, the threshold values of 50 and 210 for 300 mm/s, 40 and 220 for 200 mm/s, and 40 and 225 for 100 mm/s were used to define the W-deficient regions. For instance, at a 300 mm/s scanning speed, regions with pixels below 50 or exceeding 210 are identified as W-deficient regions (including their W-rich halo), while the matrix is taken for pixels between 50 and 210. Further microstructural investigations were carried out using a SEM coupled with energy-dispersive spectroscopy (EDS) and electron backscatter diffraction (EBSD) system (Oxford Aztec) at an accelerating voltage of 20 kV. Pure cobalt standards were used to calibrate the EDS instrument. The bulk composition of the printed sample was acquired by averaging EDS area analyses results from three equally-divided regions of cross-sectional BSE image, each about 0.8 mm × 3.5 mm in size. The matrix composition was obtained from averaging EDS point analyses results from 10 randomly chosen points. The acquired EBSD data were further post-processed using Aztec Crystal and TSL OIM 7 Analysis software.

2.4. Creep tests

To investigate the mechanical properties at high temperatures, two cylindrical compressive creep specimens (8 mm in height, 4 mm in diameter) were electro-discharge machined from built cylinders and homogenized and aged under the same conditions as above. Compressive creep tests were performed in air at 850 °C ± 3 °C, the specimens were subjected to a constant load while measuring the sample displacement rate using an extensometer and a linear variable differential transducer. After establishing and recording a steady-state strain rate, the stress is increased to a higher value and the procedure is repeated to a maximum total strain of ≈ 10%. Minimum creep strain rate was determined at each stress level after achievement of a steady-state displacement rate (Figure S2 shows creep strain vs. time curves obtained from creep tests).

3. Experimental results

3.1. As-built microstructure

Preliminary tests using blended elemental powders without milling resulted in much lower W mole fractions of 3 % to 4 % in as-built samples, which was ascribed to a non-homogeneous mixing of powders and W powder settling during powder loading in the L-PBF instrument, because of the high density of W powders. As a result, alloys created with milled powders (as described in the previous section) are exclusively described in the following. Figures 3(a-d) show BSE micrographs of alloys fused with laser scanning speed of 100 mm/s, 200 mm/s, 300 mm/s, and 400 mm/s. Sub-micron-size pores, indicated by green arrows, are expected to be gas pores, owing to their round shapes and small size. A porosity content of ≈ 0.1 % was observed in the printed samples.

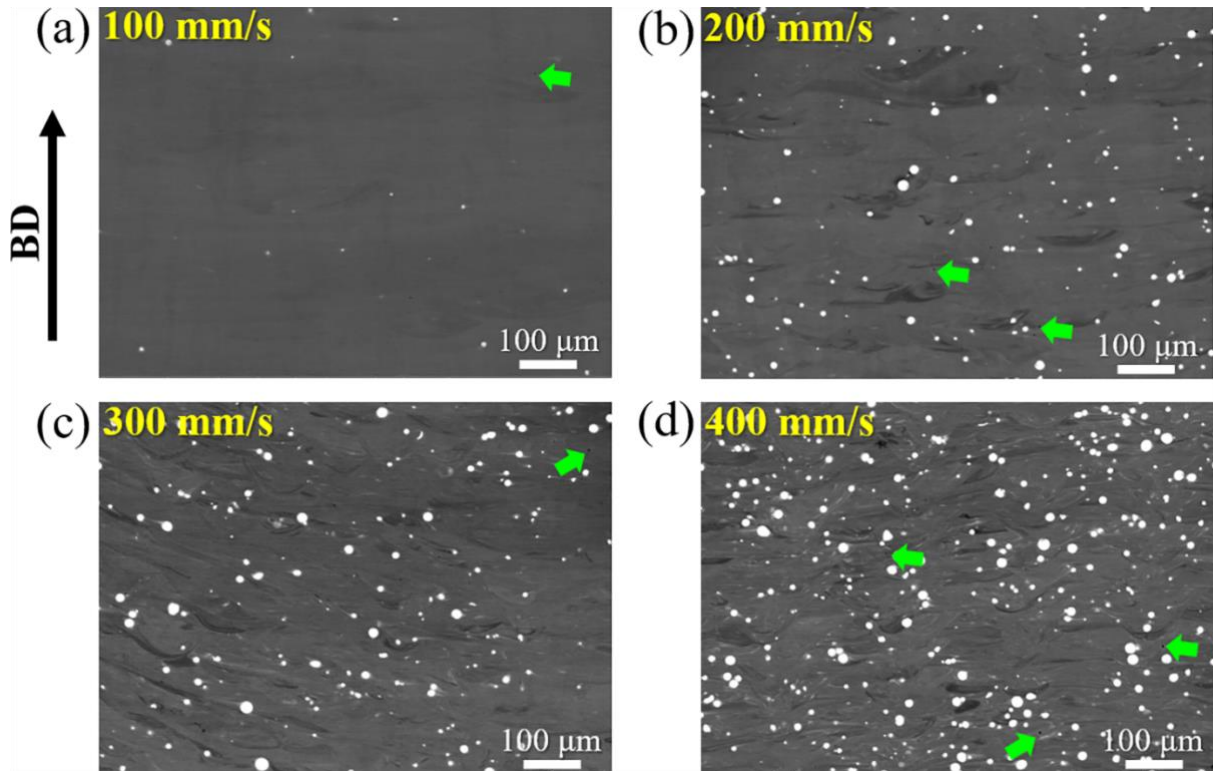


Figure 3. BSE images of as-built alloys, with scanning speed of (a) 100 mm/s, (b) 200 mm/s, (c) 300 mm/s, and (d) 400mm/s. White particles are partially-melted W powders, and darker regions are W-deficient regions. Green arrows indicate small pores.

All samples exhibit partially-melted W particles with a brighter contrast and W-deficient regions with a darker contrast than the matrix. The number density of partially-melted W particles and W-deficient regions increases with increasing scanning speed, as presented in Figure 4(a): at the highest scanning speed of 400 mm/s, the sample shows the highest fraction of a W particles (4.1 %) and W-deficient regions (15.0 %), consistent with the lowest volumetric energy density of 159 J/mm³. Figure 4(b) shows average diameter and number density (per unit area) of W particles as a function of scanning speed. The average size is constant with an average diameter, D , of $\approx 7 \mu\text{m}$, within a wide error reflecting the natural size distribution of the particle and their 2D cross-section. The number density however rises strongly, from $\rho \approx 80 \text{ mm}^{-2}$ to $\rho \approx 800 \text{ mm}^{-2}$, as the scanning speed increases from 100 mm/s to 400 mm/s.

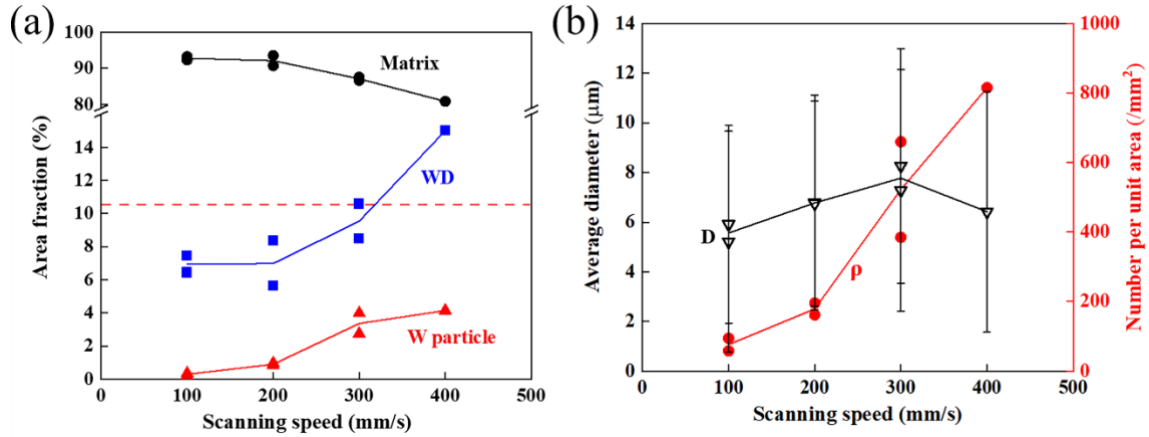


Figure 4. Evolution with laser scanning speed, in as-built alloys, of: (a) area fractions of partially-melted W particles, W-deficient regions (WD), and matrix; (b) average diameter D and number density ρ of partially-melted W particles. Lines connect average values for each scanning speed. The red dashed line in (a) indicates the area fraction of W particle (10.6 %) expected if no W melting/dissolution occurs.

The presence of partially-melted W particles in the as-built sample results in W depletion in the matrix as compared to the average W composition (Table 1). The average W mole fraction measured on cross-sections vary between 7.1 % and 8.3 % which is well within the compositional window for the γ/γ' two-phase region as predicted by the thermodynamic database. Table 1 also shows that Co, Ni, and Al concentrations, both on average (sample-wide) and within the matrix, are close to the nominal concentrations for all samples.

Table 1. Total and matrix compositions of as-built samples processed at various laser scanning speeds, obtained from EDS measurements. Compositions are given mole fraction $\times 100$.

Speed	Nominal	400 mm/s		300 mm/s		200 mm/s		100 mm/s	
		total	matrix	total	matrix	total	matrix	total	matrix
Al	11	8.9 ± 0.3	9.8 ± 1.2	10.8 ± 0.4	10.8 ± 0.7	10.6 ± 0.2	10.6 ± 0.6	10.3 ± 0.4	11.0 ± 2.1
Co	61	62.3 ± 0.7	64.5 ± 3.2	61.0 ± 0.2	61.9 ± 1.4	62.1 ± 0.4	62.0 ± 1.0	61.3 ± 0.3	60.8 ± 1.6
Ni	20	20.4 ± 0.1	21.2 ± 2.6	20.5 ± 0.1	20.7 ± 1.3	20.2 ± 0.3	20.7 ± 0.3	20.5 ± 0.2	20.5 ± 0.7
W	8	8.3 ± 0.6	4.5 ± 1.5	7.7 ± 0.4	6.7 ± 0.8	7.1 ± 0.2	6.6 ± 0.3	7.9 ± 0.3	7.7 ± 0.8

Figure 5(a) shows an EBSD micrograph of a partially-melted W particle and its surrounding matrix. The W particle exhibits a tail, surrounded with a W-enriched halo, consistent with the particle having partially melted and resolidified with incomplete mixing with the surrounding melt. As expected, the W particle and matrix exhibit BCC (Body-Centered Cubic) and FCC crystal structure, respectively; no other intermetallic phase are observed, despite numerous possible W-rich intermetallic phases (e.g., Co_3W or Co_7W_6 for Co-W), which is consistent with a rapidly dissolving W particle. In Fig. 5(b), a BSE micrograph and its EDS line-scan of elemental distribution profiles across two W particles and the surrounding matrix presents a gradually decreasing W concentration from the particle edge to the matrix. The W particles do not contain Co, Ni, and Al, confirming that they are un-melted, rather than melted and re-

solidified. The left particle also shows a bright W-rich halo, as confirmed by the line scan. This may represent W in solution in the matrix (similar to Fig. 5(a)) or the signal may originate from the W particle itself below the polished surface, if it was sectioned well above its mid-section. The strong trend of W particle size increasing with scanning speed, seen in Fig. 4(b), is consistent with higher scanning speed reducing the time when liquid Co-Ni-Al is present and thus able to dissolve W, thus increasing the size of the remaining, partially-melted W particles. Furthermore, Co, Ni and Al compositions in the matrix are quite consistent that a homogenous matrix is obtained during melting this alloy, despite incomplete W dissolution.

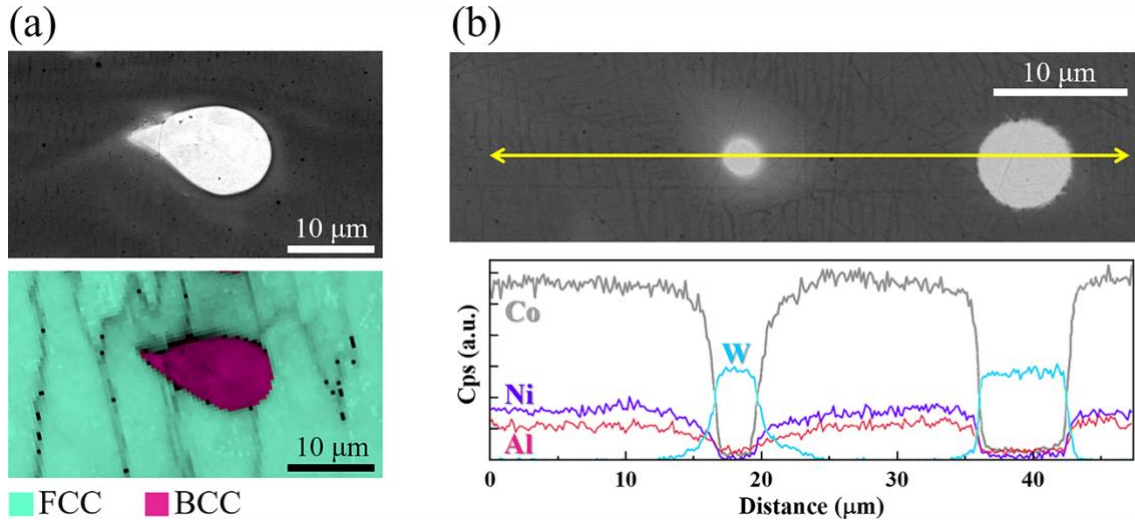


Figure 5. (a) BSE micrograph and EBSD phase map of W particle and the surrounding matrix region for as-built sample (300 mm/s scanning speed). (b) BSE micrograph and EDS line-scan composition profile across two W particles and the surrounding matrix.

Figs. 6(a-c) shows W-deficient regions from the sample produced at an intermediate scanning speed v ($v=200$ mm/s): these regions exhibit dark and non-uniform contrast, as expected if they are deficient in high-Z contrast tungsten, and compositionally inhomogeneous. Ignoring the W content from EDS results composition, the normalized local composition of various points in Figs. 6(a-c) are marked in the Co-Ni-Al phase diagram (calculated using the CHiMaD-Co thermodynamic database, Fig. 6(d)). The W content of each point is shown by the color of the symbols in the phase diagram. The star symbol marks the average composition normalized from Co-20.2Ni-10.6Al-7.1W to Co-21.7Ni-11.4Al by ignoring the W concentration, for as-built sample ($v=200$ mm/s). The black dashed lines drawn from the star parallel to each of the sides of the diagram indicate the normalized average concentration of each element. Considering the three sections in the phase diagram divided by the black dashed lines in Fig. 6(d), all points measured in Fig. 6(a-c) are located in a region which is both Co-depleted and Al-enriched (except points 2 and 3), while points 2, 3, and 5 are also Ni-enriched. Concentrations of W are well below the average alloy concentration ($W = 7.1$) consistent with the absence of other W-containing phases. While the Co concentrations are also lower than the average value, increased Al and/or Ni concentrations lead to formation of the β -(Co,Ni)Al B2 phase, while some region remain in the FCC- γ Co-Ni-Al phase. The β phase is expected to have formed during solidification and to be (sub-)micron in size, and thus not resolved in these micrographs and sufficiently small to be dissolved during homogenization. Figure 6(c) shows a rare instance of a large β -phase region with a eutectic microstructure and a Co-18Ni-22Al normalized composition (point 9) and a low W content of 3.3. The ternary composition is in

the eutectic monovariant reaction trough of the Co-Ni-Al system (20–25 Al and 0–76 Ni), as reported by Ref. [34].

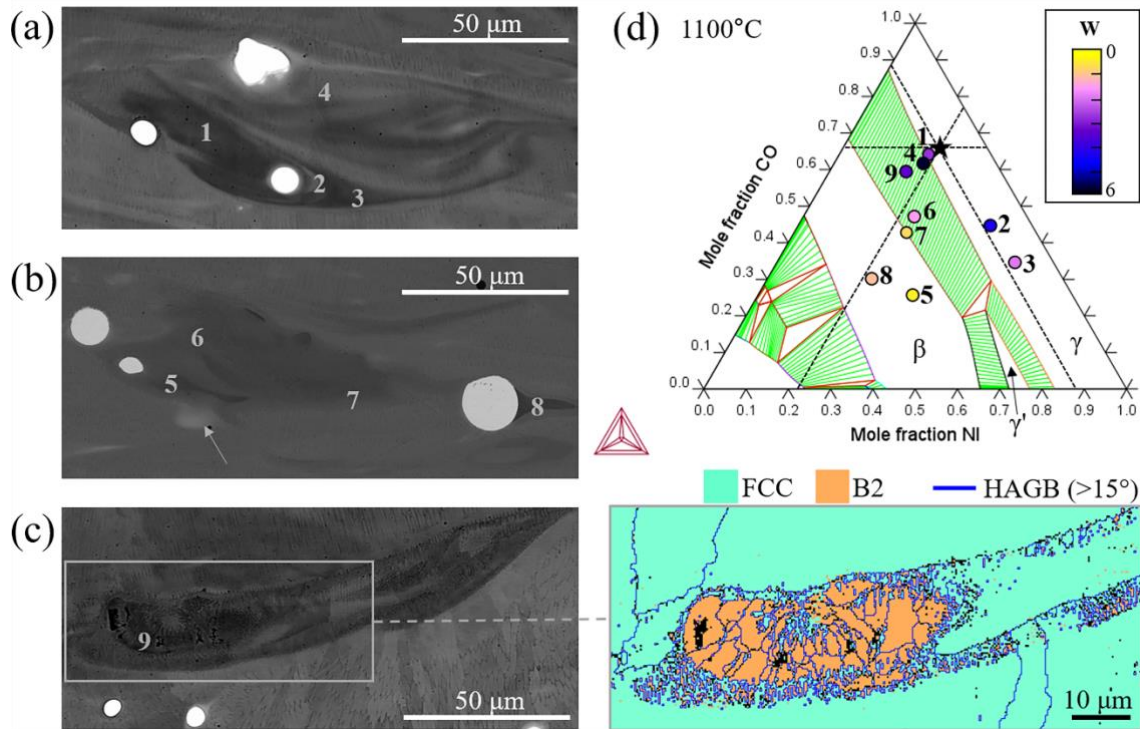


Figure 6. (a-c) Micrographs of W-deficient regions in as-built Co-20.2Ni-10.6Al-7.1W alloy (produced at 200 mm/s scanning speed), with 9 points labelled where EDS analysis was performed. (c) Enlarged view of W-deficient region and corresponding phase map. (d) Co-Ni-Al phase diagram at 1100 °C with compositions from (a-c) marked by circles color-coded based on their W concentration (see colormap); the average alloy composition of Co-21.7Ni-11.4Al is marked by a star symbol. All compositions are normalized by removing W.

3.2. Crack analysis

3.2.1. Cracks and microfeatures

Figure 7(a) shows W-deficient regions and melt pool boundaries (yellow lines) identified using an etched SEM image, indicating that W-deficient regions form inside the melt pool. Figure 7(b) shows EBSD and BSE images around W-deficient regions and cracks marked by yellow arrows. Columnar grains are present, which are often observed in alloys fabricated by additive manufacturing [17,35,36]. Cracks are located at high-angle grain boundaries (>15°) which are parallel to the build direction, and propagate along the building direction. This is expected, cracks are often observed at grain boundaries in various Ni-base superalloys manufactured via L-PBF [11,35,37,38]. The location of W-deficient regions correlates with horizontal grain boundaries.

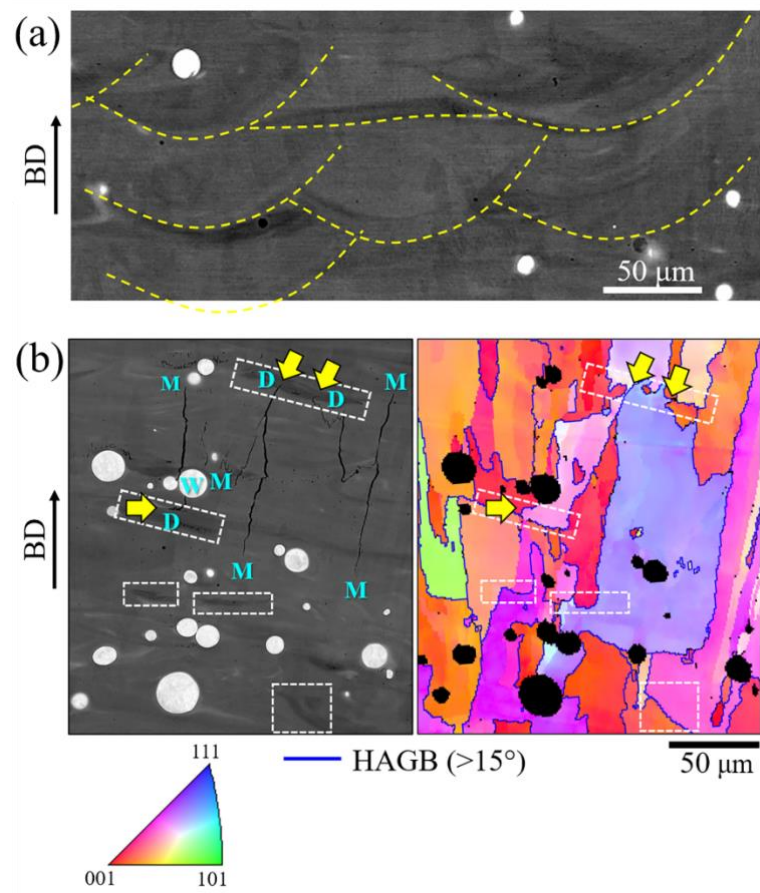


Figure 7. (a) BSE image of as-built sample ($v=200$ mm/s) with W-deficient regions areas visible, which correlate with the melt pool boundaries shown with yellow lines. (b) BSE image and EBSD inverse pole figure (IPF)-Z map of the FCC phase with high angle grain boundaries ($> 15^\circ$) marked by blue color from a sample built at higher speed, $v=300$ mm/s. Labels M for matrix, W for partially-melted W particle (white contrast), and D for W-deficient regions represent each microfeature where cracks end/start. W-deficient regions in both BSE image and IPF-Z (Inverse pole figure- Z direction) map are indicated by white dash box. Yellow arrows mark cracks (a) which end at W-deficient regions or (b) which possibly originated from the tip of W-deficient regions.

Figure 8 shows a BSE micrograph of a crack that is bridged by a partially-melted W particle. The crack width below the bridge, where the crack stops, is clearly reduced, consistent with effective bridging. The W particle appears plastically deformed by the crack and its interface with the matrix is intact, indicating strong adhesion and lack of embrittlement. This illustrates that cracks forming during L-PBF may be inhibited by the partially-melted W particles. Similar toughening by crack bridging has been reported in NiAl-W [39,40] and $(\text{Ti}_{0.5}\text{Ta}_{0.5})\text{Al-W}$ [41].

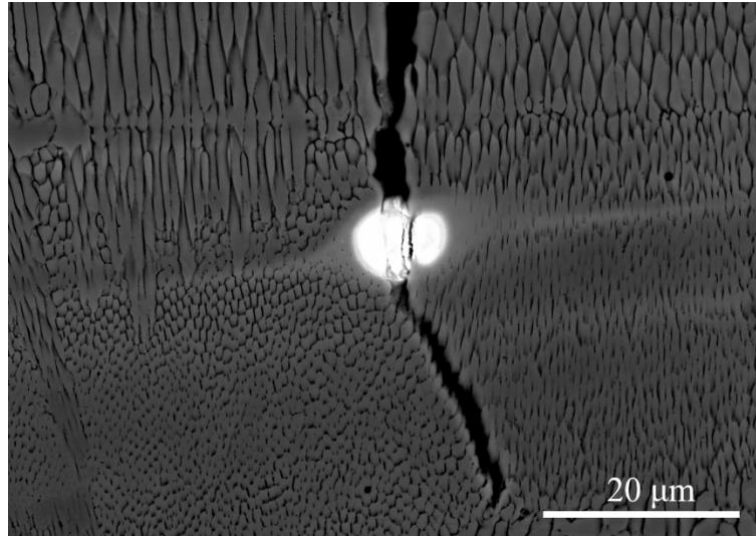


Figure 8. BSE micrograph of crack bridged by W particle in as-built alloy ($v=200$ mm/s). Matrix shows cellular microstructure, probably due to local composition deviation from the nominal value.

Figure 9 presents BSE and EBSD images of cracks in the vicinity of W particles and W-deficient regions, in a sample produced at a relatively fast 300 mm/s scanning speed. In Fig. 9(a,c), cracks propagated along the build direction and deflected at grain boundary triple junctions, including a horizontal grain boundary. The upper cyan arrow, in particular, indicates a W-deficient region located at a horizontal grain boundary. The kernel average misorientation (KAM) map suggests that this horizontal grain boundary, where the crack was deflected, shows a high strain concentration (cyan arrows, Fig. 9(b)). Many cracks stop near, or at, W particles (yellow arrows) and the crack tip region around W particle is plastically deformed (Fig. 9(b)). The strain concentrations were observed around most W particles, regardless of interactions with cracks. Also, strain concentrations were often observed within W particles (indicating plastic deformation), with some exceptions when the W particles are far from cracks.

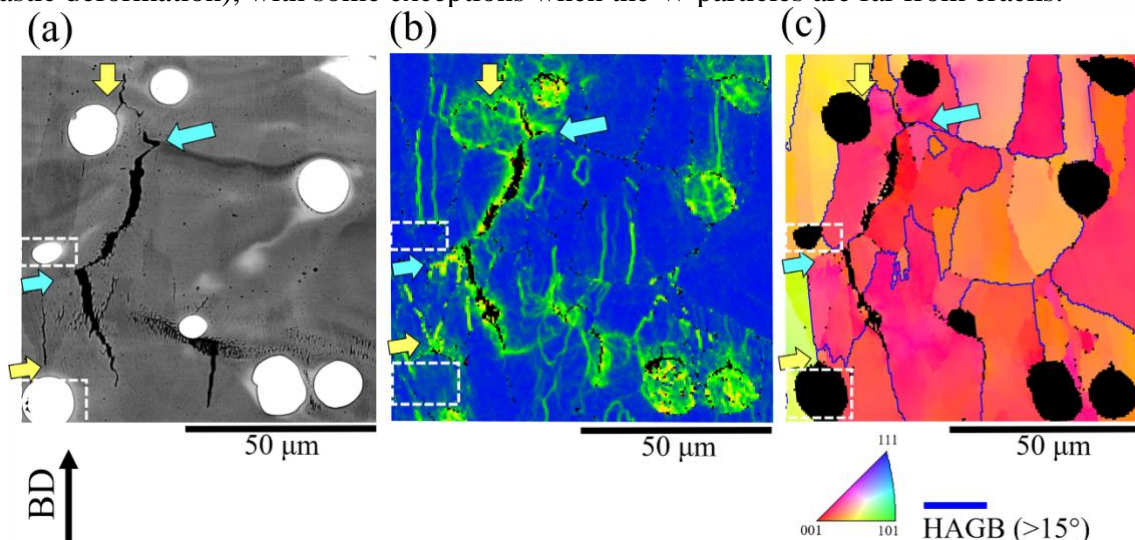


Figure 9. Microstructure of as-built alloy (rapid scanning speed, $v = 300$ mm/s) (a) BSE micrograph, (b) KAM map (maximum angle of 5°), and (c) EBSD IPF-Z map of the FCC phase with high angle grain boundaries ($> 15^\circ$) marked by the blue color. Arrows indicate regions where plastic strain is localized, near horizontal grain boundaries (cyan) and W particles

(yellow). The white dashed boxes indicate two W particles without strain concentrations inside. In (b), the black pixels at the matrix/particle interfaces are not cracks, but a shading effect of the less-deeply etched W particles.

3.2.2. Crack size measurement

Figure 10 shows that crack areal density, in the horizontal and vertical cross sections, decreases significantly with increasing scan speed. This is in accordance with research showing that cracking in L-PBF increases with decreasing scan speed, due to large thermal residual stresses and large columnar grain sizes [42,43]. The crack density is zero for the highest scan speed of 400 mm/s, but 20 lack-of-fusion events were recorded over a 21 mm² area. For 300 mm/s speed, the crack density is also very low, but it increases rapidly for the two lower speeds (100 mm/s and 200 mm/s).

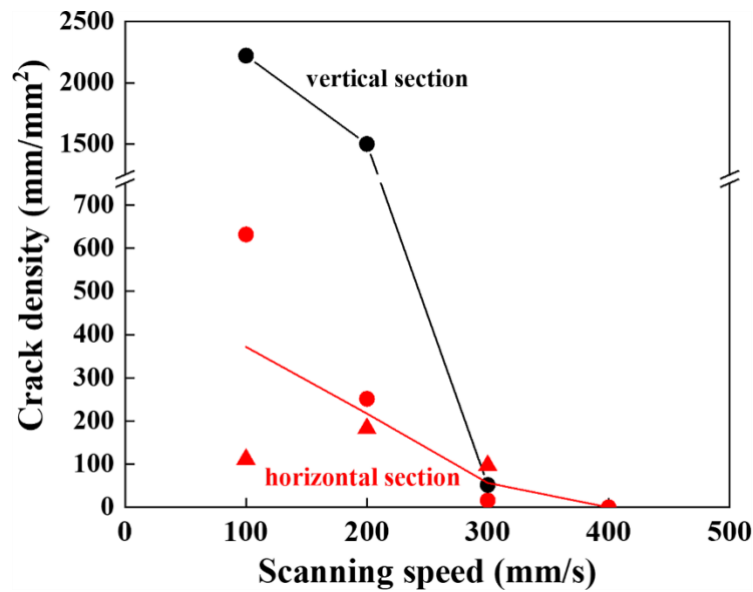


Figure 10. Dependence on laser scanning speed of crack density measured from vertical and horizontal cross-section. Red circles (horizontal cross-section) and black circles (vertical cross-section) are from the same sample. The lines connect the average density value for each scanning speed. Scale is interrupted and varies above and below 750 mm/mm².

The numbers of cracks that end/start at each microfeature (W particles, W-deficient regions, and matrix) were counted for the horizontal and vertical sections of each specimen produced at scanning speed of 100 mm/s, 200 mm/s, and 300 mm/s. Since W-deficient regions show a complex microstructure, they were divided into four cases (as illustrated in Figure 11(a)), to investigate their effect on crack occurrence and blocking: (1) WD1, for cracks propagating along the building direction that terminate at the interface between the matrix and a W-deficient region; (2) WD2, for cracks propagating and terminating along the interface between matrix and a W-deficient region; (3) WD3, for cracks propagating along the building direction but finishing within a W-deficient region; (4) WD4, for cracks propagating along the scanning direction and finishing at the interface between matrix and a W-deficient region.

Figure 11(b) addresses the end/start points of the cracks, determining their location in the above regions for the three scanning speeds. Cracks ending within the matrix are most prevalent for samples produced at the lowest scanning speed of 100 mm/s, but become less so with increasing laser scan speed. Furthermore, WD1 cracks are more likely for samples built at 200 mm/s and 300 mm/s than for the sample built at 100 mm/s. This suggests that cracks in alloys

produced at higher scanning speeds are more affected by W particles and W-deficient regions than those built at lower speeds. Cracks ending at W particles are generally less represented than those that end in the matrix and at WD1. In W-deficient regions, WD1 show the highest value and WD2 the second highest (except for vertical cross section at 100 mm/s). In Fig. 11(c), these data are normalized by the area fraction of each region. For all specimens, W particles and WD1 display higher values, as compared to the matrix and other WDs. This suggests that ductile, tough W particles and more brittle W-deficient regions may block and initiate cracks, respectively.

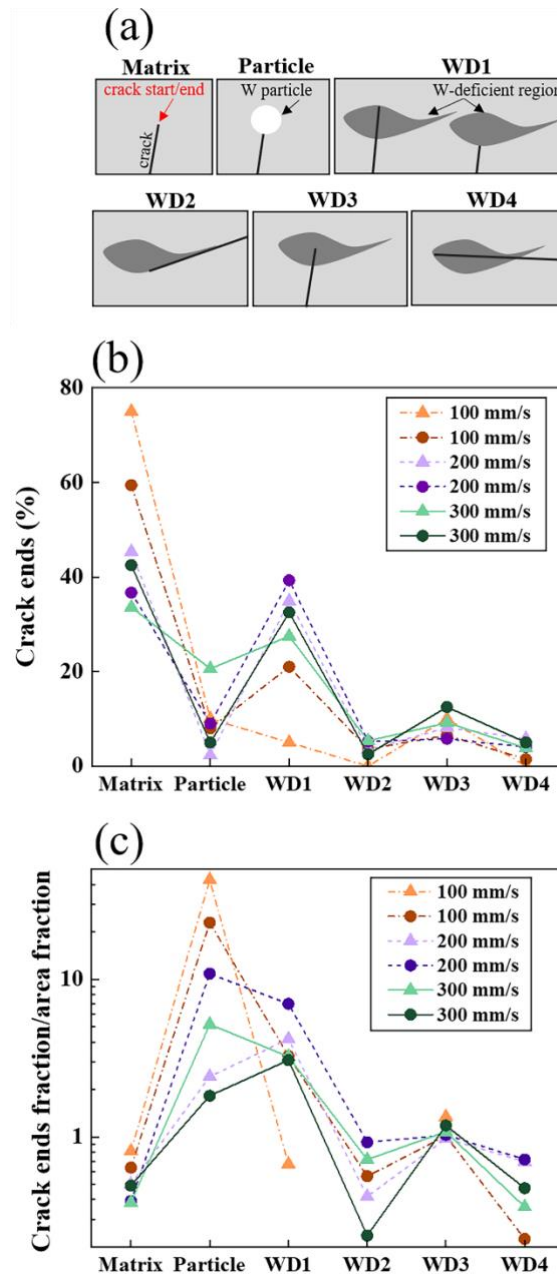


Figure 11. (a) categorization of microfeature associated with crack starts/ends at: matrix, W particle, and W-deficient regions (WD) (b) Number of cracks which start/end at each region, normalized by the total number of crack tips. (c) Fraction of crack that ends at each region, normalized by the area fraction of each region. The circle and triangle symbols in (b) and (c) correspond to the samples represented by circle and triangle, respectively, in Fig. 10.

3.2.3. Crack morphology

Figure 12(a) shows a SE image and the corresponding elemental EDS map of a cracked region from the horizontal cross-section of a sample built at the lowest scanning speed ($v = 100$ mm/s). The cracks, as observed in the horizontal cross-sections, are longer than those found in specimens built at a faster scanning speed ($v=200$ mm/s). In Fig. 12(a), the crack follows a W-enriched region within a matrix with a homogeneous distribution of all elements, due to low scanning speed. Figure 12(b) shows an etched BSE image of a horizontal cross-section of an as-built sample ($v=200$ mm/s). Melt tracks aligned along the scanning direction are visible (enclosed by blue dashed line) and longitudinal cracks (blue arrows) are observed to be confined within single melt tracks. Figure 12(c) presents calculated freezing range results with varying W concentration in Co-20Ni-8Al- x W ($x=2, 4, 6,$ and 8). The freezing range increases with increasing W concentration in this system. Changes in W concentration in the matrix with the changing scanning speed thus affects the freezing range of the matrix, and its propensity for cracking.

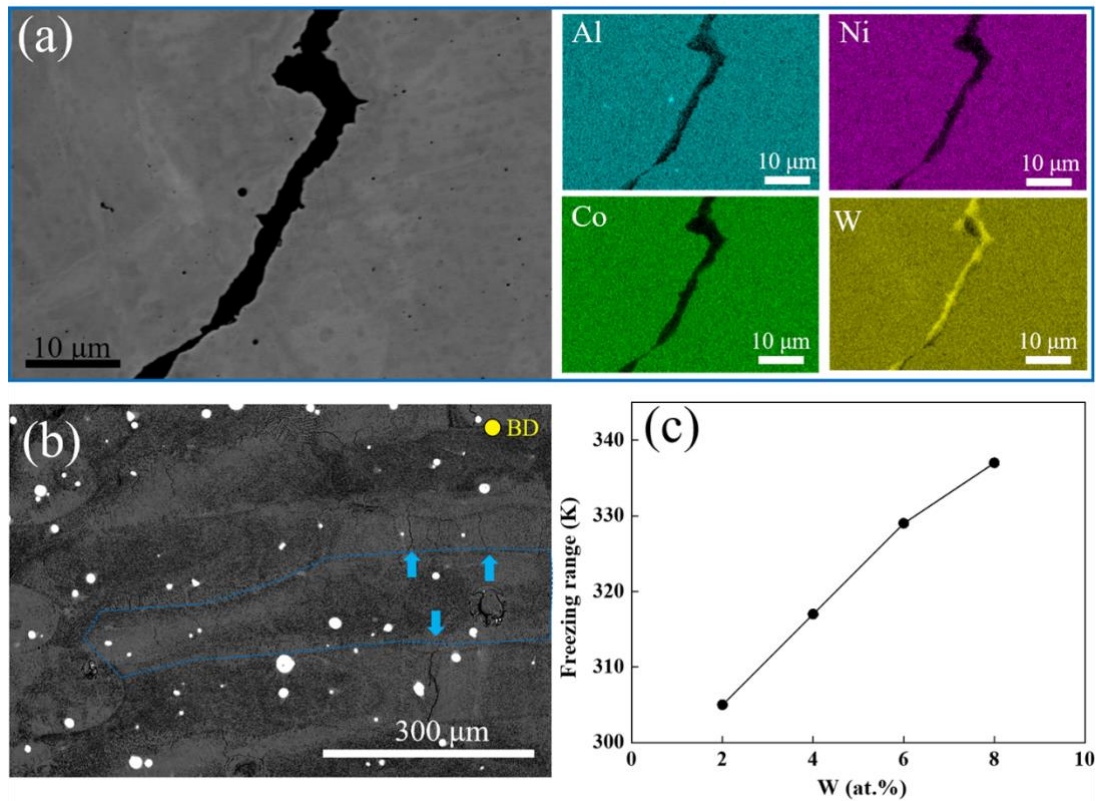


Figure 12. Microstructure of as-built alloys, with (a) SE micrograph and elemental EDS map near crack from horizontal cross-section for a slow scanning speed of 100 mm/s. (b) etched BSE micrograph from horizontal cross-section for a faster scanning speed of 200 mm/s. Blue dashed lines represent melt tracks. Blue arrows show longitudinal cracks. (c) Predicted freezing range with W concentration (x) of Co-20Ni-8Al- x W ($x=2, 4, 6,$ and 8)

Figure 13(a) shows a micrograph of two cracks (labelled C1 and C2) in a sample created at the lowest building speed ($v=100$ mm/s). The horizontal crack C1 is due to solidification cracking, judging from the dendritic morphology at its faces. An EDS line scan across crack C1 (Fig. 13(c)) shows that the region around the crack is Al-enriched and W-depleted. This may lead to solidification cracking since Al enrichment increases the freezing range (Fig. 1(a)). The

difference in Al mole fraction between the crack C1 and the matrix region is sizeable ($\approx 4\%$), as determined from EDS measurements of points A and B in Figure 13(a): Co-21.1Ni-14.8Al-6.5W and Co-20.2Ni-10.5Al-8.7W, respectively. By contrast, crack C2 (which is perpendicular to C1 and parallel to the build direction) does not show dendritic features and is thus probably formed in the solid after solidification. This is confirmed by an IPF-X map (Fig. 13(a)) showing that the crack C2 formed along a high angle grain boundary. It is possible that crack C1 (which formed first during solidification) acted as initiation sites for crack C2 [44] at the intersection with the vertical high angle grain boundary.

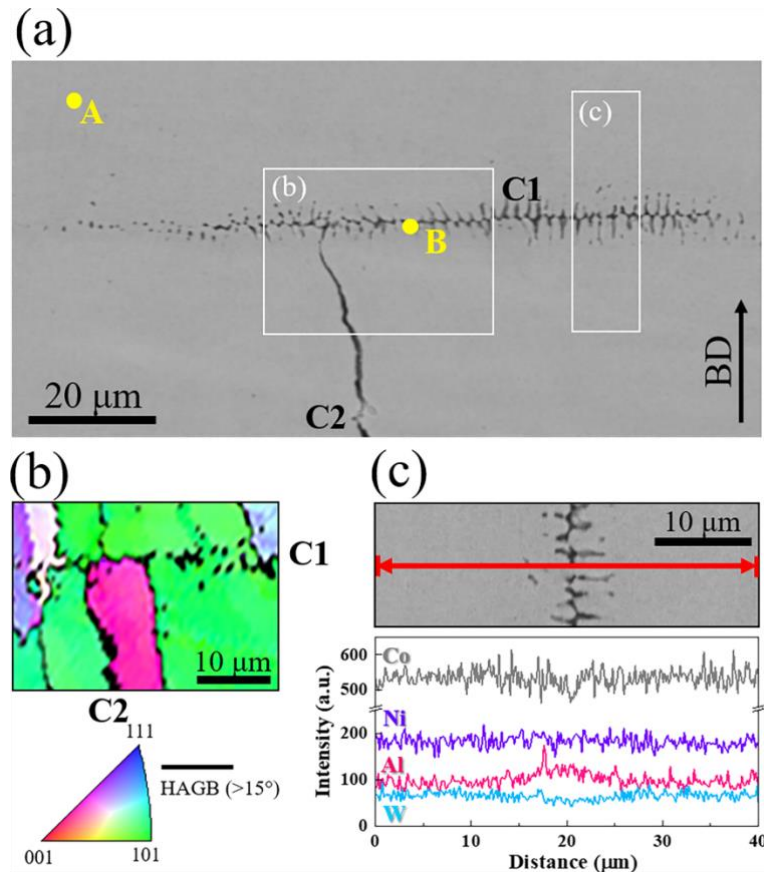


Figure 13. (a) SE image of sample produced at the lowest scanning speed (100 mm/s) showing two cracks labelled C1 and C2. (b) IPF-Z map of FCC phase showing that crack C2 follows a high-angle grain-boundary and (c) EDS line across crack C1, showing Al enrichment and W depletion.

3.3 As-homogenized and aged microstructures

Figure 14 shows a cross-section of the surface of the as-homogenized sample (built at a 300 mm/s scanning speed) in which Al (and some Ni) diffused from the NiAl powder pack used during the 1200 °C homogenization (Fig. S4) to stem Al losses by sublimation. The top diffusion layer is identified as Al-poor β -(Co,Ni)Al, based on a measured composition near the surface (in contact with NiAl powders) of Co-20Ni-34Al-2W (B2-CoAl has a very wide Al composition range, with a mole fraction as low as 27 % Al at 1200 °C [45]). Thus, the top layer in Figure 14 is equivalent to an oxidation-resistant diffusion coating [46,47]. A 200 μm thick diffusion layer between the bulk alloy and the top β -(Co,Ni)Al layer is observed, consisting of β -(Ni,Co)Al+ μ -Co₇W₆. The μ -Co₇W₆ phase forms from W rejected as Al in-diffusion forms the W-depleted β -(Co,Ni)Al layer. Below these two Al-enriched layers, the alloy exhibits a

homogenized γ -phase (Fig. S5) indicating that the partially-melted W particles and W-deficient regions present after solidification are fully dissolved after the homogenization treatment.

After removing the μ and β phases at the specimen surface, the sample (300 mm/s scanning speed) with homogeneous γ microstructure was aged at 900 °C for 24 h, resulting in formation of a two-phase γ/γ' microstructure, with no grain-boundary precipitation (Fig. 15). The size of the γ' precipitates in the grain is 150 nm to 250 nm and their volume fraction is 77 % (as determined using ImageJ), which is in reasonable agreement with the calculated predictions of 70% (Fig. 1).

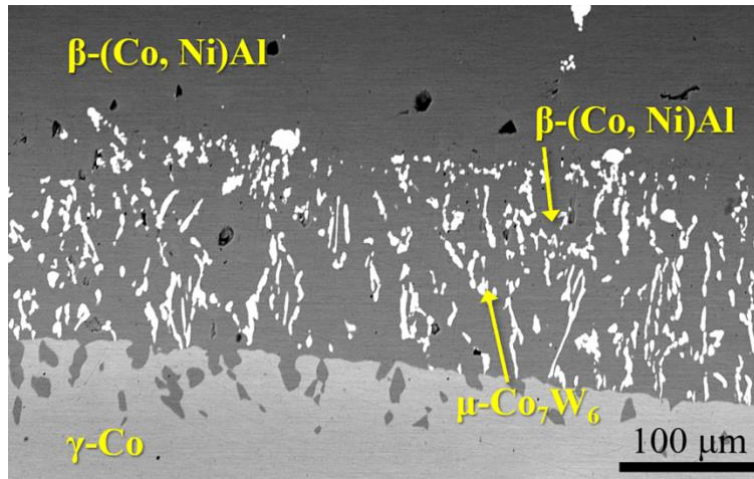


Figure 14. BSE image of homogenized alloy (built at 300 mm/s scanning speed) near sample surface which was in contact with NiAl powder (used as Al source during homogenization at 1200 °C). A W-depleted, Al-enriched β -(Co,Ni)Al region is at the specimen surface (which is outside the micrograph field of view). Below it, a W- and Al-enriched β -(Co,Ni)Al+ μ -Co₇W₆ region exists, which is in contact with the bulk unmodified region (marked γ -Co).

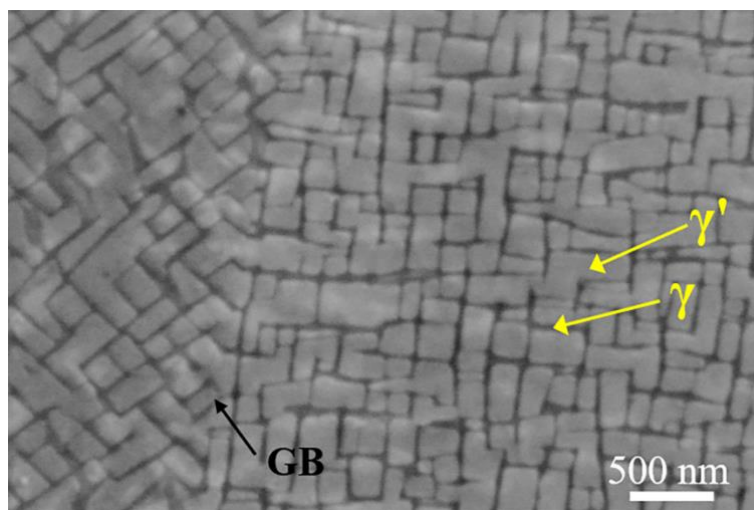


Figure 15. SEM image of sample (300 mm/s scanning speed) after homogenizing and aging at 900 °C, showing a γ/γ' microstructure in two grains separated by a grain boundary (GB).

3.4. Creep properties

Figure 16 shows, for as-homogenized and aged alloys, a double-logarithmic plot of minimum creep strain rate $\dot{\epsilon}$ vs. stress σ , as measured at 850 °C, consistent with a power-law relationship:

$$\dot{\epsilon} = A \exp\left(\frac{-Q}{RT}\right) \sigma^n \quad [1]$$

where A is a geometric pre-factor (given by material properties), Q is the creep activation energy, and n is the creep exponent. Both alloys show two creep regimes. At lower stress (below 220 MPa and 300 MPa for as-homogenized and as-aged alloys, respectively), the stress exponents n of both alloys are near unity, indicating a diffusional creep regime: the red dashed line ($n=1$) is within the estimated experimental errors of $\pm 25\%$. The grain size (50 μm to 100 μm , as measured on the aged alloy) is fine enough for diffusional creep, and it increases modestly to 100 μm to 200 μm after creep, indicating that dynamic recrystallization is not occurring.

At higher stress, increased stress exponents $n=7.5$ to $n=7.9$ are consistent with the dislocation creep regime [48–50]. Despite their similar stress exponent, the aged alloy exhibits strain rates which are about one order of magnitude lower than homogenized alloy at a given stress; this also shifts by ~ 70 MPa the transition between creep regimes (which occurs at $4 \times 10^{-8} \text{ s}^{-1}$). This improvement in creep resistance is attributed to the strengthening effect of the γ' precipitates formed during aging. The as-aged alloy also shows lower minimum strain rates than a Co-12Al-8W alloy fabricated by DED [13], but significantly higher rates than as-cast Co-9Al-9W-0.12B, whose grain boundaries are strengthened with B additions [48]. Finally, the stress exponent of cast, aged Co-9Al-9W-0.12B [49] is similar ($n=9.6$), and the creep rates in the dislocation regime are similar to our aged alloy. By contrast, cast, aged Co-9.5Al-7.5W [51] shows much faster creep (due to the lower content of γ' formers), but a similar stress exponent.

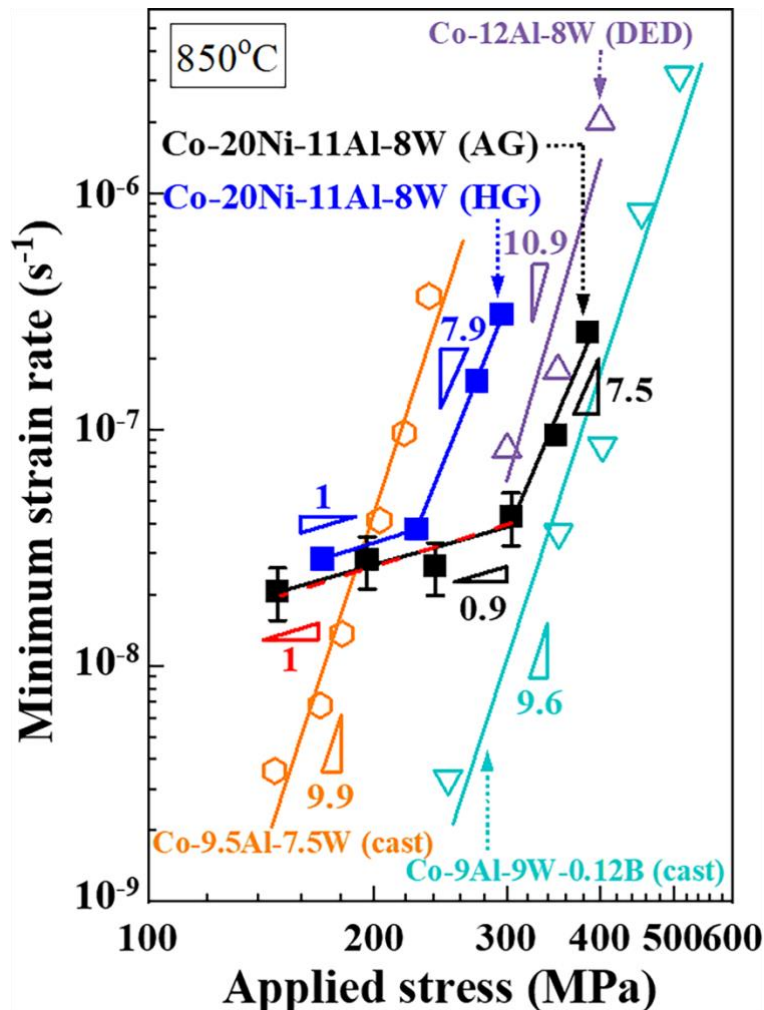


Figure 16. Double-logarithmic plot of minimum strain rate vs. compressive stress and stress exponent n of homogenized sample (denoted as Co-20Ni-11Al-8W (HG)) and aged sample (denoted as Co-20Ni-11Al-8W (AG)) at 850 °C. The open data points are data from references: Co-12Al-8W (DED) [13], Co-9.5Al-7.5W (cast) [51], and Co-9Al-9W-0.12B (cast) [49]. Red dashed line represents the stress exponent of $n=1$. The data points of as-aged alloys below 300 MPa are shown with error bars estimated as $\pm 25\%$. Stress exponent n are given next to each best fit line.

4. Discussion

4.1. Cracks in horizontal cross-sections

The sample built at the lowest scanning speed ($v=100$ mm/s) shows solidification cracking (Fig. 12(a)) with W segregation at the crack. This is consistent with W being rejected to interdendritic regions during solidification and the remaining W-rich liquid film forming solidification cracks as it cannot withstand the strain [52]. As a low scanning speed melts most of the W particles, the W matrix mole fraction is very close to nominal mole fraction (7.7 % W vs. 7.9 % W, Table 1). This high W concentration may lead to an increased freezing range and thus a high solidification cracking tendency. Even though the W concentration in the matrix increases by only 1% mole fraction as the scanning speed increases from 100 mm/s to 300 mm/s, the effect is non-linear.

The much higher crack density in horizontal cross-section of samples built with 100 mm/s and 200 mm/s scanning speeds (Fig. 10) might be associated with the melt track overlap ratio and the hatch spacing [53]. The horizontal cross section for $v=200$ mm/s exhibits longitudinal cracks. Some cracks were observed to be confined within single melt track, while others propagate further. When considering the melt pool width for $v=200$ mm/s (≈ 120 μm , Fig. 12(b)) and a hatch spacing of 105 μm in this work, the overlap ratio is 12.5 %; this may not be sufficient to ensure remelting of the previously-deposited adjacent track [54]. Another possible reason for the high preponderance of cracks in horizontal cross-section is the anisotropic distribution of cracks that are much longer than then the width. Unlike the horizontal cross-sections, vertical cross-sections may not intersect some of the vertically-oriented cracks form at high angle grain boundaries of columnar grains oriented along the building direction.

4.2. Microfeatures in as-deposited microstructures

The absence of W-rich intermetallic phases (e.g., Co_3W , $\mu\text{-Co}_7\text{W}_6$, NiW_2) at the interface between the partially-melted W particles and the surrounding Co- and Ni-rich matrix can be explained by the very rapid cooling of the melt in the L-PBF process. Marangoni convection drives the rapid movement of the W particles, which dissolve in the super-heated Co-Ni-Al melt too rapidly to form intermetallic phases, leaving a W-enriched “tail” visible as bright swirls in the as-solidified microstructures (Fig. 5(a)). The time available for homogenization of W-rich liquid pockets with the surrounding melt is too short to achieve a homogenous W distribution after solidification, so the local composition melt is preserved by the rapid solidification [55].

In the as-melted state, Co, Ni, and Al in the melt near partially-melted W particles appear to be prevented from mixing completely due to the presence of W particles (see Fig. 6). In fact, partially-mixed regions with non-uniform contrast were mainly observed to form near, or contain, partially-melted W particle, thus becoming W-deficient due to incomplete melting of the W particle. This incompletely homogenized state is preserved by rapid solidification, with

distinct areas enriched with Co, Ni, and Al observed within W-deficient region, indicating that insufficient time is available for homogeneous liquid mixing. Additionally, columnar grains grow along the build direction due to the steep vertical temperature gradient during L-PBF process [44]. The temperature gradient ahead of the solidification front can vary due to local composition differences, and thus locally changing solidus and liquidus temperatures. This local inhomogeneity in composition and temperature gradient may trigger grain nucleation [44], whose orientation may differ from the grains growing at the solidification front, thus forming a horizontal grain boundary. These horizontal grain boundaries are often observed underneath (Fig. S3), or at, W-deficient regions.

These W-deficient regions affect initiation and propagation of cracks *via* several mechanisms: (i) *Crack propagation is blocked or its main direction (along the building direction) is deflected by W-deficient regions (WD1)*. The plastic strain concentration at horizontal grain boundaries deflects cracks (Fig. 9(b) and Fig. S3). From Fig. 11(b), horizontal cross sections show more WD1 instances than the vertical cross sections, which might indicate that vertical cracks are more affected by W-deficient region than horizontal cracks.

(ii) *Cracks initiate at the interface of W-deficient regions (WD2)*. When Al is particularly enriched near the edge of a W-deficient region, solidification cracking can occur and cracks propagate along the interface with the help of a horizontal grain boundary (as shown in Fig. 13).

(iii) *Solidification cracking occurs due to the widened freezing range of Al-enriched region (WD3 and WD4, Fig. 13)*. When the Al composition in W-deficient region is about 12 % to 17 % mole fraction, it is insufficient for B2 formation but still higher than the matrix value, thus delaying termination of solidification in W-deficient region due to widened freezing ranges. As seen in Fig. 13(a), this solidification cracking can provoke initiation of new cracks in the solid state, by forming W-deficient regions (WD3).

(iv) *Crack initiates from the tip of a brittle B2 region in W-deficient regions (WD3 and WD4)*. The B2 phase formation is attributed to Al enrichment in W-deficient regions (Al > 17 % mole fraction). Both solidification and solid-state cracking are feasible from the brittle B2 phase. Solid-state cracking can be enhanced by thermal expansion and modulus mismatches, and the incoherent interface between the FCC-matrix and the B2 phase during heating and cooling. Furthermore, higher enrichment of Al (Al > 20 % mole fraction) can induce an eutectic reaction (Fig. 6(c)), with formation of large amounts of the B2 phase. Since this eutectic microconstituent has low melting point, liquation cracking is also possible, as well as solidification- and solid-state cracking.

4.3. Ductile phase toughening

The presence of partially-melted W elemental powder may provide ductile phase toughening, arresting cracks and increasing the fracture toughness [39,56,57]. The interaction between W particles and cracks follow three scenarios in our samples. First, cracks finish at (near) the interfaces of W particles and matrix (yellow arrows in Fig. 9). When normalizing by area, this is a high-occurrence event (Fig. 11(c)) indicating that W particles are effective crack arresters. Second, cracks penetrate W particles that act as ductile bridges (Fig. 8). A well-bonded interface between the particle and the surrounding matrix allow plastic deformation the W particles [56]. Finally, cracks are deflected by W particles (Fig. S3), with the high stiffness of W retarding crack approach towards W particles [56].

Crack blocking (Fig. 9) or deflecting (Fig. S3) is accompanied by strain concentrations around W particles (but often within them). The presence of localized strain both out- and inside particles without interface fracture suggests that BCC-W is ductile enough to accommodate

propagation of cracks by plastic deformation, (Fig. 8) [58], especially if cracking occurs above the ductile to brittle transition temperature of tungsten (DBTT = 200 °C to 250 °C, [59]). On the other hand, W particles without a strain concentration in their volumes were observed to block cracks, resulting in strain concentrations in the matrix (the yellow arrow the left below of Fig. 9). This suggests that W is elastically deformed and that cracks may be arrested in some instance without W plastic deformation (e.g., below their DBTT).

5. Conclusions

A quaternary Co-based superalloy, with Co-20Ni-11Al-8W composition, was chosen for laser powder bed fusion (L-PBF) processing, based on CALPHAD-based thermodynamic predictions for a moderate freezing range (to minimize cracking) and high γ' volume fraction (for creep resistance). Rather than prealloyed powders, a blend of ball-milled elemental powders was used during L-PBF, with the following results obtained:

1. In the as-fused state, the alloy exhibits a mostly-homogenous composition which nevertheless contains partially-melted W particles and W-deficient regions. Compositional segregation and more partially-melted W-particles are observed with increasing laser scanning speed, consistent with shorter melt lifetimes preventing full W dissolution in the melt.
2. W-deficient regions, which are also Ni- and Al-enriched, nucleate grains with grain boundaries perpendicular to the building direction. They may also act as both a crack-initiating and crack-deflecting sites. An enrichment of Al, in particular, induces formation of B2-(Co,Ni)Al, even eutectic microconstituents, further generating cracks.
3. Partially-melted W particles are effective at arresting or bridging cracks, as illustrated by crack density decreasing with increasing laser scanning speed (and thus increasing fraction of partially-melted W particles). Thus, W particles may provide ductile phase toughening and increase fracture toughness during the L-PBF process. The strain concentration around W particles accompanies arresting cracks, indicating that W is ductile enough to accommodate propagation of cracks.
4. These two W-rich and W-deficient features disappear after heat-treatment at 1200 °C, as W diffusion leads to full homogenization of the alloy. Subsequent aging at 900 °C leads to a γ/γ' microstructure with a 77 % volume fraction of γ' precipitates, in general agreement with thermodynamic predictions.
5. Under compressive creep deformation at 850 °C, homogenized alloys, with and without aging to achieve the γ/γ' microstructure, exhibit dislocation-controlled creep at high stresses and diffusional creep at low stresses (consistent with their relatively fine grain size of 50 μm to 100 μm). A substantial decrease in minimum creep strain rate in the dislocation creep regime is ascribed to the precipitation strengthening effect of the γ' phase.

Acknowledgments - This study was supported by the U.S. Department of Commerce, National Institute of Standards and Technology, as part of the Center for Hierarchical Materials Design (CHiMaD) at Northwestern University via award 70NANB14H012. The authors acknowledge Mr. Chuan Liu (NU) for preliminary calculations related to Fig. 1. This work made use of the MatCI Facility which receives support from the MRSEC Program (NSF DMR-1720139) of the Materials Research Center at Northwestern University; and the EPIC facility of Northwestern University's NUANCE Center, which received support from the Soft and Hybrid Nanotechnology Experimental (SHyNE) Resource (NSF ECCS-1542205). The authors

gratefully acknowledge Dr. Carla Shute (NU) for experimental assistance in the MatCI facility. HJI is thankful to Dr. Jennifer Glerum and Mr. Clement Ekaputra for their help with using the Sisma instrument.

References

- [1] A. Suzuki, H. Inui, T.M. Pollock, L12-strengthened Cobalt-base superalloys, *Annu. Rev. Mater. Res.* 45 (2015) 345–368.
- [2] Y. Zhao, Y. Zhang, Y. Zhang, Y. Luo, D. Tang, H. Liu, H. Fu, Deformation behavior and creep properties of Co-Al-W-based superalloys: A review, *Prog. Nat. Sci. Mater. Int.* 31 (2021) 641–648.
- [3] S.K. Makineni, M.P. Singh, K. Chattopadhyay, Low-density, high-temperature Co base superalloys, *Annu. Rev. Mater. Res.* 51 (2021) 187–208.
- [4] C.S. Lee, Precipitation-hardening characteristics of ternary Cobalt - Aluminum - X Alloys, The University of Arizona, 1971. <http://hdl.handle.net/10150/287709>.
- [5] J. Sato, T. Omori, K. Oikawa, I. Ohnuma, R. Kainuma, K. Ishida, Cobalt-base high-temperature alloys, *Science*. 312 (2006) 90–91.
- [6] H. Mughrabi, The importance of sign and magnitude of γ/γ' lattice misfit in superalloys - with special reference to the new γ' -hardened cobalt-base superalloys, *Acta Mater.* 81 (2014) 21–29.
- [7] J. Zhu, M.S. Titus, T.M. Pollock, Experimental Investigation and Thermodynamic Modeling of the Co-Rich Region in the Co-Al-Ni-W Quaternary System, *J. Phase Equilibria Diffus.* 35 (2014) 595–611.
- [8] V.A. Vorontsov, J.S. Barnard, K.M. Rahman, H.Y. Yan, P.A. Midgley, D. Dye, Coarsening behaviour and interfacial structure of γ' precipitates in Co-Al-W based superalloys, *Acta Mater.* 120 (2016) 14–23.
- [9] H. Yan, V.A. Vorontsov, D. Dye, Alloying effects in polycrystalline γ' strengthened Co-Al-W base alloys, 6811 (2013).
- [10] E.A. Lass, Application of Computational Thermodynamics to the Design of a Co-Ni-Based γ' -Strengthened Superalloy, *Metall. Mater. Trans. A.* 48 (2017) 2443–2459.
- [11] C. Kenel, A. De Luca, S.S. Joglekar, C. Leinenbach, D.C. Dunand, Evolution of Y2O3 dispersoids during laser powder bed fusion of oxide dispersion strengthened Ni-Cr-Al-Ti γ/γ' superalloy, *Addit. Manuf.* 47 (2021) 102224.
- [12] S. Ghorbanpour, J. Bicknell, M. Knezevic, Fatigue strength of additive manufactured Mar-M-509 superalloy, *Mater. Sci. Eng. A.* 840 (2022) 142913.
- [13] B. Yoo, C. Jung, K. Ryou, W.S. Choi, L. Haußmann, S. Yang, T. Boll, S. Neumeier, P. Choi, Directed energy deposition of γ/γ' Co-Al-W superalloys, *Addit. Manuf.* 60 (2022) 103287.
- [14] M.H. Mosallanejad, B. Niroumand, A. Aversa, A. Saboori, In-situ alloying in laser-based additive manufacturing processes: A critical review, *J. Alloys Compd.* 872 (2021) 159567.
- [15] S. Griffiths, H. Ghasemi Tabasi, T. Ivas, X. Maeder, A. De Luca, K. Zweiacker, R. Wróbel, J. Jhabvala, R.E. Logé, C. Leinenbach, Combining alloy and process modification for micro-crack mitigation in an additively manufactured Ni-base superalloy, *Addit. Manuf.* 36 (2020).
- [16] J.U. Rakhmonov, C. Kenel, A. De Luca, C. Leinenbach, D.C. Dunand, Effect of Y2O3 dispersoids on microstructure and creep properties of Hastelloy X processed by laser powder-bed fusion, *Addit. Manuf. Lett.* 3 (2022) 100069.
- [17] D. Tomus, P.A. Rometsch, M. Heilmaier, X. Wu, Effect of minor alloying elements on crack-formation characteristics of Hastelloy-X manufactured by selective laser melting,

- Addit. Manuf. 16 (2017) 65–72.
- [18] J. Ma, L. Jia, W. Jia, F. Jin, In-situ alloyed medium entropy alloy fabricated by laser powder bed fusion: microstructure and cryogenic performance, *Adv. Eng. Mater.* (2022).
- [19] P. Chen, X. Yao, M.M. Attallah, M. Yan, In-situ alloyed CoCrFeMnNi high entropy alloy: Microstructural development in laser powder bed fusion, *J. Mater. Sci. Technol.* 123 (2022) 123–135.
- [20] J. Wang, Y. Wang, Y. Su, J. Shi, Evaluation of in-situ alloyed Inconel 625 from elemental powders by laser directed energy deposition, *Mater. Sci. Eng. A.* 830 (2022) 142296.
- [21] M. Dang, J. Yu, X. Lin, H. Chai, H. Ding, H. Tan, W. Huang, Formation mechanism and thermal stability of γ' and γ'' compact co-precipitated nanostructure in directed energy deposited Ni-based alloy, *Mater. Charact.* 194 (2022) 112450.
- [22] W. Wei, J.C. Xiao, C.F. Wang, Q. Cheng, F.J. Guo, Q. He, M.S. Wang, S.Z. Jiang, C.X. Huang, Hierarchical microstructure and enhanced mechanical properties of SLM-fabricated GH5188 Co-superalloy, *Mater. Sci. Eng. A.* 831 (2022) 142276.
- [23] N.C. Ferreri, S. Ghorbanpour, S. Bhowmik, R. Lussier, J. Bicknell, B.M. Patterson, M. Knezevic, Effects of build orientation and heat treatment on the evolution of microstructure and mechanical properties of alloy Mar-M-509 fabricated via laser powder bed fusion, *Int. J. Plast.* 121 (2019) 116–133.
- [24] S.P. Murray, K.M. Pusch, A.T. Polonsky, C.J. Torbet, G.G.E. Seward, N. Zhou, S.A.J. Forsik, P. Nandwana, M.M. Kirka, R.R. Dehoff, W.E. Slye, T.M. Pollock, A defect-resistant Co–Ni superalloy for 3D printing, *Nat. Commun.* 11 (2020) 4975.
- [25] D.N. Yoon, W.J. Huppmann, Chemically driven growth of tungsten grains during sintering in liquid nickel, *Acta Metall.* 27 (1979) 973–977.
- [26] O. Dinçer, M.K. Pehlivanolu, N.K. Çalışkan, I. Karakaya, A. Kalkanli, Processing and microstructural characterization of liquid phase sintered tungsten-nickel-cobalt heavy alloys, *Int. J. Refract. Met. Hard Mater.* 50 (2015) 106–112.
- [27] P. Wang, W. Xiong, U.R. Kattner, C.E. Campbell, E.A. Lass, O.Y. Kontsevoi, G.B. Olson, Thermodynamic re-assessment of the Al-Co-W system, *Calphad.* 59 (2017) 112–130.
- [28] C. Campbell, G. Lindwall, K. Moon, M. Williams, W. Tso, Development of a Diffusion Mobility Database for Co-based Superalloys, *Materialsdata.nist.gov*, 2022. <https://hdl.handle.net/11256/998>.
- [29] F. Yan, W. Xiong, E.J. Faierson, Grain structure control of additively manufactured metallic materials, *Materials.* 10 (2017) 1260.
- [30] Y. Ro, Y. Koizumi, H. Harada, High temperature tensile properties of a series of nickel-base superalloys on a γ/γ' tie line, *Mater. Sci. Eng. A.* 223 (1997) 59–63.
- [31] T. Murakumo, Y. Koizumi, K. Kobayashi, H. Harada, Creep Strength of Ni-Base Single-Crystal Superalloys on the γ/γ' Tie-Line, *Superalloys 2004.* (2004) 155–162.
- [32] H.Y. Yan, V.A. Vorontsov, J. Coakley, N.G. Jones, H.J. Stone, D. Dye, Quaternary Alloying Effects and the Prospects for a New Generation of Co-Base Superalloys, *Superalloys 2012.* (2012) 705–714.
- [33] K. Shinagawa, T. Omori, J. Sato, K. Oikawa, I. Ohnuma, R. Kainuma, K. Ishida, Phase equilibria and microstructure on γ' phase in Co-Ni-Al-W system, *Mater. Trans.* 49 (2008) 1474–1479.
- [34] Y. Zhou, P. Nash, S.M. Bessa, G.T. Ferrigatto, B.S.V.P. Madureira, A.S. Magalhães, A. Oliveira, G.C. Pereira, L.G. Ribeiro, L.P. dos Santos, A.A. da Silva, J.D. Silva, A.G. Silva, J.M. de Souza, Y.S. Torres, R.L. da Silva, B.F.R.F. de Cunha, Phase Equilibria in the Al-Co-Ni Alloy System, *J. Phase Equilibria Diffus.* 38 (2017) 630–645.
- [35] Q. Han, Y. Gu, R. Setchi, F. Lacan, R. Johnston, S.L. Evans, S. Yang, Additive

- manufacturing of high-strength crack-free Ni-based Hastelloy X superalloy, *Addit. Manuf.* 30 (2019) 100919.
- [36] S. Wu, H.Y. Song, H.Z. Peng, P.D. Hodgson, H. Wang, X.H. Wu, Y.M. Zhu, M.C. Lam, A.J. Huang, A microstructure-based creep model for additively manufactured nickel-based superalloys, *Acta Mater.* 224 (2022) 117528.
- [37] H. Wang, L. Chen, B. Dovgyy, W. Xu, A. Sha, X. Li, H. Tang, Y. Liu, H. Wu, M.S. Pham, Micro-cracking, microstructure and mechanical properties of Hastelloy-X alloy printed by laser powder bed fusion: As-built, annealed and hot-isostatic pressed, *Addit. Manuf.* 39 (2021) 101853.
- [38] Y. Chen, K. Zhang, J. Huang, S.R.E. Hosseini, Z. Li, Characterization of heat affected zone liquation cracking in laser additive manufacturing of Inconel 718, *Mater. Des.* 90 (2016) 586–594.
- [39] R. Asthana, R. Tiwari, S.N. Tewari, Compressive properties of zone-directionally solidified β -NiAl and its off-eutectic alloys with chromium and tungsten, *Mater. Sci. Eng. A.* 336 (2002) 99–109.
- [40] R. Tiwari, S.N. Tewari, R. Asthana, A. Garg, Mechanical properties of extruded dual-phase NiAl Alloys, *J. Mater. Sci.* 30 (1995) 4861–4870.
- [41] H.E. Dève, M.J. Maloney, On the toughening of intermetallics with ductile fibers: Role of interfaces, *Acta Metall. Mater.* 39 (1991) 2275–2284.
- [42] C. Guo, S. Li, S. Shi, X. Li, X. Hu, Q. Zhu, R.M. Ward, Effect of processing parameters on surface roughness, porosity and cracking of as-built IN738LC parts fabricated by laser powder bed fusion, *J. Mater. Process. Technol.* 285 (2020) 116788.
- [43] L.N. Carter, M.M. Attallah, R.C. Reed, Laser powder bed fabrication of nickel-base superalloys: Influence of parameters; characterisation, quantification and mitigation of cracking, *Superalloys 2012 Proc. Int. Symp. Superalloys.* (2012) 577–586.
- [44] Z. Zhou, L. Huang, Y. Shang, Y. Li, L. Jiang, Q. Lei, Causes analysis on cracks in nickel-based single crystal superalloy fabricated by laser powder deposition additive manufacturing, *Mater. Des.* 160 (2018) 1238–1249.
- [45] A.J. McAlister, The Al-Co (Aluminum-Cobalt) system, *Bull. Alloy Phase Diagrams.* 10 (1989) 646–650.
- [46] A.E. Paz y Puente, D.C. Dunand, Effect of Cr content on interdiffusion and Kirkendall pore formation during homogenization of pack-aluminized Ni and Ni-Cr wires, *Intermetallics.* 101 (2018) 108–115.
- [47] D. Erdeniz, D.C. Dunand, Microstructure development during pack aluminization of nickel and nickel-chromium wires, *Intermetallics.* 50 (2014) 43–53.
- [48] D.J. Sauza, D.C. Dunand, D.N. Seidman, Microstructural evolution and high-temperature strength of a γ (f.c.c.)/ γ' (L12) Co–Al–W–Ti–B superalloy, *Acta Mater.* 174 (2019) 427–438.
- [49] A. Bauer, S. Neumeier, F. Pyczak, R.F. Singer, M. Göken, Creep properties of different γ' -strengthened Co-base superalloys, *Mater. Sci. Eng. A.* 550 (2012) 333–341.
- [50] A. Sharma, C. Mondal, S.K. Makineni, K. Chattopadhyay, D. Banerjee, Exploring the correlation between microscopic mechanisms and macroscopic behaviour in creep of a directionally solidified tungsten-free γ/γ' CoNi-base superalloy, *Acta Mater.* 228 (2022) 117738.
- [51] B.J. Peter, *Microstructure and Mechanical Properties in Gamma(face-centered cubic) + Gamma Prime(L12) Precipitation-Strengthened Cobalt-based Superalloys*, Northwestern University, 2015.
- [52] H.E. Sabzi, S. Maeng, X. Liang, M. Simonelli, N.T. Aboulkhair, P.E.J. Rivera-Díaz-del-Castillo, Controlling crack formation and porosity in laser powder bed fusion: Alloy

- design and process optimisation, *Addit. Manuf.* 34 (2020) 101360.
- [53] P. Rebesan, M. Ballan, M. Bonesso, A. Campagnolo, S. Corradetti, R. Dima, C. Gennari, G.A. Longo, S. Mancin, M. Manzolaro, G. Meneghetti, A. Pepato, E. Visconti, M. Vedani, Pure molybdenum manufactured by Laser Powder Bed Fusion: Thermal and mechanical characterization at room and high temperature, *Addit. Manuf.* 47 (2021) 102277.
- [54] Y. Cao, H.L. Wei, T. Yang, T.T. Liu, W.H. Liao, Printability assessment with porosity and solidification cracking susceptibilities for a high strength aluminum alloy during laser powder bed fusion, *Addit. Manuf.* 46 (2021) 102103.
- [55] T. Zhang, Z. Huang, T. Yang, H. Kong, J. Luan, A. Wang, D. Wang, W. Kuo, Y. Wang, C.T. Liu, In situ design of advanced titanium alloy with concentration modulations by additive manufacturing, *Science*. 374 (2021) 478–482.
- [56] F.E. Heredia, M.Y. He, G.E. Lucas, A.G. Evans, H.E. DEVE, D. Konitzer, The fracture resistance of directionally solidified dual-phase NiAl reinforced with refractory metals, *Acta Metall. Mater.* 41 (1993) 505–511.
- [57] K.S. Ravichandran, A survey of toughness in ductile phase composites, *Scr. Metall. Mater.* 26 (1992) 1389–1393.
- [58] M.Y. He, F.E. Heredia, D.J. Wissuchek, M.C. Shaw, A.G. Evans, The mechanics of crack growth in layered materials, *Acta Metall. Mater.* 41 (1993) 1223–1228.
- [59] P.L. Raffo, Yielding and fracture in tungsten and tungsten-rhenium alloys, *J. Less-Common Met.* 17 (1969) 133–149.